Antibody-based donor-acceptor spatial reconfiguration in decorated lanthanide-doped nanoparticle colloids for the quantification of okadaic acid biotoxin

Filip Stipić,[a] Petra Burić,[a] Željko Jakšić,[a] Galja Pletikapić,[b] Maja Dutour Sikirić,[c] Goran Zgrablić,[d] Leo Frkanec,[e] Daniel M. Lyons [a,*]

[a] Center for Marine Research, Ruđer Bošković Institute, G. Paliaga 5, 52210 Rovinj, Croatia.

[b] Department of Marine and Environmental Research, Ruđer Bošković Institute, Bijenička cesta 54, 10000 Zagreb, Croatia.

[c] Department of Physical Chemistry, Ruđer Bošković Institute, Bijenička cesta 54, 10000 Zagreb, Croatia.

[d] Time Resolved X-Ray Spectroscopy Laboratory, Elettra-Sincrotrone Trieste, 34149 Basovizza, Italy.

[e] Department of Organic Chemistry and Biochemistry, Ruđer Bošković Institute, Bijenička cesta 54, 10000 Zagreb, Croatia.

* to whom correspondence may be addressed: E-mail: lyons@irb.hr, Fax: +385 52 804780; Tel: +385 52 804725

Abstract

With the increasing movement away from the mouse bioassay for the detection of toxins in commercially harvested shellfish, there is a growing demand for the development of new and potentially field-deployable tests in its place. In this direction we report the development of a simple and sensitive nanoparticle-based luminescence technique for the detection of the marine biotoxin okadaic acid. Photoluminescent lanthanide nanoparticles were conjugated with fluorophore-labelled anti-okadaic acid antibodies which, upon binding to okadaic acid, gave rise to luminescence resonance energy transfer from the nanoparticle to the organic fluorophore dye deriving from a reduction in distance between the two. The intensity ratio of the fluorophore : nanoparticle emission peaks was found to correlate with okadaic acid concentration, and the sensor showed a linear response in the 0.37–3.97 μM okadaic acid range with a limit of detection of 0.25 μM. This work may have important implications for the development of new, cheap and versatile biosensors for a range of biomolecules and that are sufficiently simple to be applied in the field or at point-of-care.

Introduction

Okadaic acid (9,10-Deepithio-9,10-didehydroacanthifolicin), an ionophore-like poly-ether derivative of a 38 carbon fatty acid, is an important molecule widely used in studies of cell growth and functioning as it is a potent serine/threonine protein phosphatase 2A inhibitor [1], [2] and [3]. Apart from its cytotoxicity and being a tumor promoter, okadaic acid also presents other risks to human health through direct ingestion. This lipophilic cyclic polyether is widely produced in the marine environment by dinoflagellates and is introduced into the

food chain through accumulation in shellfish which, upon consumption, results in diarrhetic shellfish poisoning [4]. The current reference method used to test for okadaic acid and other marine biotoxins is the mouse bioassay, a controversial method as results may be equivocal, suffers from low sensitivity and specificity, and ends with the death of the animal. Thus, the European Union and the World Health Organization have directed that the use of laboratory animals be phased out with a call for states to improve and validate new toxin detection methods in shellfish [5] and [6]. However, as the okadaic acid acute reference dose is three to four times lower than the current regulatory limit of 160 μg kg^{-1}, expected future reductions in the latter will also require more sensitive analytical techniques to be developed as the detection limit of such techniques must be several times lower than any new regulatory limit [7]. While the enzyme linked immunosorbent assay (ELISA) has proven a sensitive technique for the detection of okadaic acid, the technique gives equal weight to toxin congeners even though their toxic potential may be different [8]. Alternatively, the development of the protein phosphatase inhibition assay allows the determination of total potential toxicity although the method is non-specific and cross-reactivity with toxin variants can occur [9]. Liquid chromatography has provided a reliable, standardized method although is limited by being restricted to a few reference laboratories, is expensive and the requirement of extensive preparatory work such as the derivatization of toxins and method calibration significantly increases the amount of time needed for samples to be analyzed [10].

While all techniques offer both advantages and disadvantages, they are generally characterized by low throughput hence there is increasing interest in developing biosensor-based approaches as they offer a solution to current drawbacks in terms of simplicity, speed and cost and ultimately may be used for analysis on-site [11] and [12]. In this direction, a number of approaches have been developed, including electrochemical immunosensors [13]

and [14], kinetic exclusion assays [15], chemiluminescence immunosensors [16] and surface plasmon resonance-based immunoassays [17]. As an alternative path, taking advantage of the unique optical properties of nanoscale materials may provide a new way in which to detect specific target molecules. A key technique which has been developed and applied extensively over the past two decades is Főrster resonance energy transfer (FRET), a mode which, by changes in spatial proximity between donor and acceptor complexes, allows non-radiative energy transfer between the two resulting in enhanced or reduced fluorescence emission at specific wavelengths. The extreme sensitivity of FRET to low target concentrations, and down to single molecules in cases, is already known [18].

Lanthanide ions have been gaining use over the past number of years, particularly in the form of chelates, as luminescent probes in biology due to their long excited-state lifetimes related to f-electron transitions which are well-shielded from external perturbations and do not participate greatly in chemical bonding [19] and [20]. As an extension of this, lanthanide ions encapsulated in nanoparticles may provide the same advantageous optical characteristics as chelates such as narrow excitation and emission lines and large Stokes shift, but with enhanced chemical stability, ease of synthesis and higher quantum yields than the organic fluorophores. Further, the long excited-state lifetimes enables time-resolved luminescence measurements which allow short-lived background fluorescence to be separated from the target signal [21], [22] and [23].

In the present work we show that lanthanide nanoparticles may be functionalized and applied to the detection of the environmental biotoxin okadaic acid by measurement of the emission of an acceptor organic dye following enhanced luminescence resonance energy

transfer (LRET) from the nanoparticle donor due to closer spatial proximity upon okadaic acid - anti-okadaic acid antibody binding.

Experimental

Materials

All chemicals except for cerium nitrate were obtained from Sigma Aldrich at the highest purity available and were used as received. Cerium nitrate (≥99% p.a.) was supplied by Fluka, while rabbit polyclonal anti-okadaic acid antibodies and AlexaFluor488 goat anti-rabbit labelling kit were supplied by Abcam (Cambridge, UK) and Life Technologies, respectively. A certified reference material comprising of blue mussel *Mytilus edulis* digestive gland tissue and a small amount of the dinoflagellate *Prorocentrum lima* containing 10.1 µg g^{-1} okadaic acid was obtained from the National Research Council of Canada.

Nanoparticle synthesis

The synthesis of amino-functionalized cerium/terbium doped LaF$_3$ nanoparticles followed the method of Diamente et al. [24] with some modifications. Briefly, a 2 mL aqueous solution of La(NO$_3$)$_3$·6H$_2$O (1.26 mmol), Ce(NO$_3$)$_3$·6H$_2$O (1.34 mmol) and Tb(NO$_3$)$_3$·6H$_2$O (0.56 mmol) was added dropwise to a 25 mL aqueous solution of *o*-phosphorylethanolamine (1 mmol; which had been initially neutralized by NH$_4$OH) and NaF (3 mmol) at 40°C. The reaction was held at this temperature for 24 h upon which acetone was added to precipitate the nanoparticles. The nanoparticles were collected by centrifugation (4500 × g, 10 min.), washed with acetone and centrifuged again.

Nanoparticle functionalization

Typically, for conjugation of anti-okadaic acid antibodies to lanthanide nanoparticles, 5 μL rabbit serum containing IgG anti-okadaic acid antibodies was added to 1 mL borate buffer solution (pH 8.0, 0.05 M) in which 1 mg LaNP (~4 nM) had been previously dispersed and was gently mixed for 1 h at room temperature. To this solution was added 15 μL goat anti-rabbit IgG F_{ab} fragment conjugated with AlexaFluor488 (AF) fluorophore and blocking reagents, and the solution was mixed for 1 h. Okadaic acid potassium salt (M_w=843.1 g mol^{-1}) was dissolved in ultrapure water and added in 10 μL aliquots (100 ng aliquot^{-1}) to the nanoparticle-antibody-F_{ab}-AF solution to give a solution with increasing okadaic acid concentration. This solution was gently mixed at room temperature for 1 h upon which it was interrogated by fluorescence spectroscopy.

Sensor validation

The sensor was subsequently validated using a range of concentrations of okadaic acid extracted from certified shellfish tissue. Mussel tissue homogenate (50-300 mg) was extracted twice with 2 mL portions of 80% methanol, with the okadaic acid-containing methanol fraction separated from the homogenate by centrifugation (1000 × g, 10 min.) The volume was reduced to 100 μL by rotary evaporation upon which 900 μL of the sensor solution was added. The solutions were gently mixed for 10 min. followed by interrogation by fluorescence spectroscopy. (Note that contact with okadaic acid may induce nausea, vomiting and diarrhoea, thus requiring appropriate protective measures be taken.)

Instrumental analysis

Powder X-ray diffraction data were collected on a Rigaku Ultima IV multi-purpose diffractometer in parafocusing mode using Cu Kα radiation of wavelength 1.5418Å, 40 kV

tube voltage, 40mA current, scan speed of 1° min^{-1} (2θ) and step size of 0.02° (2θ). Divergence, receiving and scattering slits of ⅔°, ⅔° and 0.3 mm were used, while a Ni filter was employed to remove Kβ radiation with a 5º Soller slit for beam shape. Data processing was done on Rigaku PDXL 2.0 software. Dynamic light scattering data were collected on a Zetasizer Nano ZS (Malvern, UK) instrument equipped with a green laser (532 nm). Samples were suspended in borate buffer solution (pH 8.0, 0.05M) and were measured at 25ºC in 1 cm PMMA cuvettes. Intensity of scattered light was detected at the angle of 173º. Samples were interrogated a minimum of 10 times and data processing was carried out on proprietary Zetasizer software 6.32 (Malvern Instruments) with results reported as number size distributions and distribution widths. Atomic force micrographs were obtained on a Multimode AFM with Nanoscope IIIa controller (Bruker, Billerica USA) with a vertical engagement (JV) 125 μm scanner, in tapping mode using silicon tips (RTESP, Bruker, nominal tip radius 8 nm). Prior to imaging samples were sonicated for 15 min., diluted to 20 μg mL^{-1}, and 5 μL of this suspension was pipeted directly onto freshly cleaved mica. Mica sheets were placed in enclosed Petri dishes for 15 min to allow samples to settle and adsorb to the surface and the surfaces were then rinsed three times with 50 μL ultrapure water and placed in enclosed Petri dishes. The excess of suspension was removed by absorption by laboratory paper. Processing and analysis of images was done on NanoScope^{TM} software (Digital Instruments, v.614r1). Scanning electron microscopy secondary electron images were recorded on a JEOL JSM 7000F instrument operating at an accelerating voltage of 10kV. Samples were prepared by allowing a drop of an aqueous dispersion of nanoparticles to gradually dry directly on the sample stub. Luminescence data were collected on a Cary Eclipse fluorescence spectrophotometer and Kontron SFM25 spectrofluorometer at room temperature using 1 cm optical path quartz cuvettes, with samples dispersed in borate buffer solution (pH 8, 0.05 M). Time resolved luminescence lifetime measurements were recorded

using the third harmonic of a 1 kHz laser system (Coherent Inc.), consisting of a Ti:SA oscillator (Mira Seed) and a Ti:SA amplifier (Legend), delivering an excitation pulse at 266 nm at a laser repetition rate of 100 Hz. The excitation beam had a diameter of 300 μm at the position of the sample and its intensity was adjusted to 15 μW so that the fluorescence intensity of the nanoparticles lay within the linear regime. The samples had OD 0.6 at 266 nm. The fluorescence was collected with a lens (f=150 mm) and focused to an amplified silicon photodiode (Thorlabs PDA36A-EC). The photodiode signal was acquired with a digital oscilloscope (Tektronix TDS3054B) that averaged out 512 shots.

Results and Discussion

Characterization of as-synthesized nanoparticles

Powder X-ray diffraction data for the cerium/terbium doped lanthanide fluoride nanoparticles showed reflections consistent with hexagonal lanthanum fluoride (LaF_3) and could be matched to the corresponding pattern in the database of the International Centre for Diffraction Data (card no. 00-008-0461; P63/mcm, a=7.184Å, c=7.351Å, α=90º, γ=120º), as shown in Figure 1. Crystallite sizes were determined by whole pattern fitting with pseudo-Voigt shaped peaks and an average crystallite size of 2.1 nm was found by applying of the Scherrer formula to six main reflections. However, due to the broad reflections and relatively low signal-to-noise, the fitting of the raw data by simulation should be considered qualitative rather than quantitative.

Decoration of nanoparticles

Nanoparticle sizes determined by atomic force microscopy in tapping mode were found to range from about 10-30 nm with a calculated average size of 24±5 nm (n=40; Figure 2a). Very small particulates of ≤1 nm were also found to be present and are ascribed to the amine

ligand, a large excess of which had been used in the synthesis to ensure a crowded nanoparticle surface that promotes upright adsorption of the antibody by the hydrophobic F_c region. AFM imaging of the lanthanide nanoparticles conjugated to anti-okadaic acid antibodies showed larger entities with sizes typically in the range from 50-70 nm (Figure 2b) while imaging of antibodies alone showed sizes of about 3 nm (Figure 2c).

Scanning electron microscopy images of nanoparticles and antibody-coated nanoparticles, respectively, are shown in Figure 3. Drying of samples prior to imaging resulted in a large degree of agglomeration, with undecorated nanoparticles forming clusters in the range of $0.5 - 1\,\mu m$ (Figure 3a) and antibody-functionalized nanoparticles agglomerating into larger structures of $1 - 4\,\mu m$ in diameter (Figure 3b). Surface morphology features are distinctly different between the as-synthesized and functionalized nanoparticles, with the latter showing a more indented surface likely related to the organic moieties residing on the surface that result in less symmetrical packing of nanoparticles during sample dehydration.

Both as-synthesized and functionalized nanoparticles showed excellent stability in aqueous media and hydrodynamic diameters were determined by dynamic light scattering of solution-dispersed samples based on the peak maxima of the number size distributions, with representative data being given in Figure 4. Anti-okadaic acid antibodies and lanthanide nanoparticles showed diameters of 10.1±1.0 nm and 15.7±2.3 nm, respectively, while nanoparticles conjugated to anti-okadaic acid antibodies and labelled with F_{ab}-Alexafluor488 showed an increase in diameter to 50.8±9.2 nm, and are consistent with AFM data. Upon binding of okadaic acid to the antibody a peak maximum was noted at 78.8±7.7 nm, showing the gradually increasing hydrodynamic diameter as the complex became larger.

The number of antibodies that form a corona around each nanoparticle and held by non-covalent interactions may be estimated by the equation [25]:

$$N_{max} = 0.65(r^3_{complex} - r^3_{nanoparticle})/r^3_{antibody}$$

Considering a hydrodynamic radius for the antibody of 5.05 nm, and close to the IgG (M_w ~150 kDa) radius of 5.41 nm reported elsewhere [26], a nanoparticle radius of 7.85 nm and complex radius of 25.40 nm, the number of antibodies around a nanoparticle is calculated to be 83. However, it should be noted that the hydrodynamic radius taken for the antibody does not take into consideration the F_{ab} fragment (M_w ~47 kDa, r_H = 2.91 nm) bound to the antibody F_c region, hence the number of antibody molecules around the nanoparticle would be expected to be less than that calculated. In addition, the difference in radius between the complex and nanoparticle of 17.55 nm is nearly 2 times the hydrodynamic diameter of the antibody alone. Thus, if arrangement of antibodies about the nanoparticle is reasonably compact, up to two layers of antibodies may be estimated as surrounding each nanoparticle with the layer closest to the nanoparticle estimated as comprising of approximately 10 protein molecules based on simple geometrical considerations. As antibodies are more loosely held in the outer layer it is possible that there is some exchange with those free in solution. Such dynamic exchange is unlikely to affect antibodies immediately bound to the nanoparticle but may facilitate the approach of okadaic acid antigen to those more tightly held LRET-enabling antibodies at the nanoparticle surface.

For other systems such as ubiquitin (M_w ~8.5 kDa) on 12 nm-diameter gold nanoparticles, the orientation of proteins has been shown to be non-random with specific domains favoring binding to the nanoparticle [27]. In that work, up to 140 proteins in the

protein corona around each nanoparticle was estimated compared to approximately 80 proteins per corona in the present work although this would be expected considering that immunoglobulin IgG has a 17 times greater molecular mass. With respect to the number of proteins closely held to the nanoparticle surface, a similar sized protein α-bungarotoxin (M_w ~8 kDa) on 20 nm $YEuVO_4$ nanoparticles showed a broad number distribution with a maximum for the coupling ratio distribution found for 3 proteins per nanoparticle [28]. From simple geometrical considerations, the number of IgG molecules in the near-surface layer in the present work was estimated at about 10 molecules per nanoparticle which is similar to the value of 7.7 IgG molecules per nanoparticle, based on the value of 2.5 mg IgG m^{-2} for typical monolayer coverage cited elsewhere [29].

Photoluminescence and fluorescence spectra

Photoluminescence and fluorescence spectra for the nanoparticle donor and fluorophore acceptor are presented in Figure 5. The spectroscopic properties of lanthanide nanoparticles derive from *f-f* transitions in partially filled 4*f* orbitals which are well shielded by filled 5*s* and 5*p* orbitals. These *f-f* transitions are forced (induced) electric dipole transitions, i.e. parity forbidden, although Laporte's parity selection rule is relaxed when the lanthanide ion becomes influenced by crystal or ligand field interactions [30]. This is particularly relevant for Tb^{3+} ions near the nanoparticle surface which lie in a more asymmetric crystal field, thus increasing the transition probability and hence intensity [24]. Doping of nanoparticles with cerium was done due to cerium being able to act as a sensitizer because of its ease of excitation in the UV region and its quick transfer of energy to an adjacent terbium atom which by itself would not be efficiently excited to a resonance level (20430 cm^{-1}; molar absorption coefficient typically less than 10 $M^{-1} cm^{-1}$) [31]. Further, the use a lanthanum fluoride nanoparticle as a rigid host matrix for the cerium ion 'antenna' and terbium ion emitter has an

important benefit over using more traditional lanthanide chelates in that the local environment is essentially free from high-energy vibrations and the Tb^{3+} centres are shielded from solvent molecules which would efficiently quench luminescence through non-radiative energy dissipation by vibronic coupling to the vibrational states of harmonic oscillators such as O-H bonds [32]. This, and the large Stokes shift between excitation and emission bands, make these doped lanthanide fluoride nanoparticles an appropriate, bright and stable photoluminescence source for exciting the organic dye. The trivalent terbium shows two emission lines, at 487 nm ($^5D_4 \rightarrow ^7F_6$) and 544nm ($^5D_4 \rightarrow ^7F_5$), the former showing excellent spectral overlap with the excitation band of AF fluorophore (Figure 5). The emission band of AF at 516 nm lies between the emission bands of the lanthanide nanoparticles with relatively little overlap hence indicating that this selected donor-acceptor pair is appropriate for investigating luminescence resonance energy transfer.

The fluorescence emission spectrum, using an excitation wavelength of 282 nm, was recorded for the nanoparticle-antibody-F_{ab}-AF-okadaic acid complex and the intensity ratio of the AF emission maximum at 516 nm to the nanoparticle luminescence emission maximum at 487 nm is given in Figure 6a. For increasing concentrations of okadaic acid the ratio of the emission peaks increased, i.e. relative emission from the AF increased while the emission from the nanoparticles decreased. Further, to ensure that no components of the complex were causing unwanted emission at 516 nm, various configurations were interrogated at an excitation wavelength of 282 nm and the spectra are presented in Figure 6b. For the nanoparticles alone, nanoparticle-antibody and nanoparticle-antibody-F_{ab}-AF combinations essentially no signal was detected at 516 nm while the addition of okadaic acid to the sensor caused an increase in emission intensity from the AF at 516 nm.

The luminescence resonance energy transfer between donor and acceptor derived from antibody-antigen binding is represented schematically in Scheme 1. In the absence of okadaic acid antigen, the distance between nanoparticle donor and fluorophore acceptor is too great to allow non-radiative energy transfer between the two and hence only the emission band of the nanoparticle is seen. Upon addition of okadaic acid and its binding to the antibody based on structural complementarity, the change in the spatial orientation of the acceptor with respect to the donor was enough to sufficiently reduce the distance between the two and allow resonance energy transfer to occur. Since the orientation of the antibody or the goat anti-rabbit F_{ab}-conjugated AF had not been expected to change greatly with respect to the nanoparticle in the presence of okadaic acid, especially if the antibody corona is reasonably well packed, achieving a LRET signal upon antibody-okadaic acid binding indicates that even very minor changes in spatial orientation may allow LRET to occur, particularly at donor-acceptor distances which border on the range in which LRET may be achieved.

Because of the extreme sensitivity of LRET to distance where energy transfer is inversely proportional to the sixth power of the distance between nanoparticle and organic dye, and low intensity signals found in this work, it is likely that only labelled antibodies in the first coordination sphere of the protein corona are sufficiently close to enable resonance energy transfer from the nanoparticle to the acceptor. Considering that the antibodies have a hydrodynamic diameter of more than 10 nm, it is likely that the organic dye lay just beyond the outer limit of distance over which LRET may occur in the absence of okadaic acid, while the addition of okadaic acid may disrupt the spatial configuration of the complex just sufficiently to bring the organic dye within distance of the nanoparticle over which energy transfer may be expected.

While IgG antibodies comprise of very specific sequences which determine their affinity and selectivity towards other macromolecules, the shape of immunoglobulin IgG is not rigid but displays great flexibility at the hinge region allowing the two F_{ab} segments to move independently. In addition, the ability of the junction of the V (variable) and C (constant) domains to rotate and bend provides even more flexibility to the point that it is referred to as a molecular 'ball and socket joint'. It is this combined flexibility at the tethered F_{ab} arms and V-C junction that plays a key role and likely facilitates sufficient shortening of the distance between the donor and acceptor upon antigen binding which results in the resonance energy transfer seen here [33]. Further, as energy is transferred only over relatively short distances it is not necessary to remove unreacted reagents from the solution thus making the measurement a simple and fast 'mix-and-shake' method.

As an alternative scenario, where the binding of the okadaic acid to its antibody results in some disruption with the labelled F_{ab} fragment becoming free and then reacting with the NP to give resonance energy transfer is not considered likely as the F_{ab} fragment is purposely designed to have high specificity and strong attraction for the primary antibody while leaving the binding sites of the antibody unhindered. Therefore it would be very unusual for it to become free of the primary antibody under the reaction conditions employed in our work. Even if such a case did arise and the binding of okadaic acid caused LRET by freeing the F_{ab}-AF fragment rather than causing LRET due to a slight conformation change of the anti-okadaic acid antibody, the result would be expected to be qualitatively the same. However, there is no evidence that the F_{ab}-AF fragment strongly interacts with the nanoparticles in the absence of anti-okadaic acid antibodies (and with or without okadaic acid) as there was no fluorescence signal from AF when exciting the nanoparticle thus indicating the lack of resonance energy transfer (discussed later in the text).

An important aspect to the achieving of LRET was the optimal orientation of antibodies on the nanoparticle surface where use of a large excess of ligand created a crowded environment which promoted the outward orientation of the bioactive and more hydrophilic F_{ab} region. To confirm this, use of ten times less ligand resulted in a sensor showing LRET even in the absence of antigen (Figure 6c), clearly indicating that in a less crowded environment the antibodies may orient themselves such that their F_{ab} region, and hence also the attached goat anti-rabbit F_{ab}-AF fragment, comes sufficiently close to the nanoparticle to enable resonance energy transfer.

Lanthanide transitions have a large energy gap (e.g. $^5D_4 \rightarrow {}^7F_0$ $\Delta E=14800cm^{-1}$) which disfavors non-radiative de-excitation processes and give rise to very long-lived excited states with lifetimes on the millisecond scale [34], as also shown in the present work and discussed later. Such long life times in time-gating experiments allow the avoidance of signal collection from direct excitation of the fluorophore. AlexaFluor488 organic dye has a short fluorescence lifetime of ~4 ns allowing separation of direct excitation from nanoparticle-derived excitation by simply collecting data more than 4 ns after excitation pulse and as a consequence significantly improving signal to noise ratios compared to steady-state illumination experiments. This means sensitivity gains that can allow measurements even down to the single nanoparticle level [35]. In the present work luminescence lifetime data were collected with a 0.1 ms delay after nanoparticle excitation at UV wavelength (Figure 7). Both individual nanoparticles and the complex comprising anti-okadaic acid antibody–nanoparticle–F_{ab}-AF–okadaic acid showed luminescence decays which could be modelled by bi-exponential fits by restricting the fitting interval to 0.1–9.7 ms. The fast and slow components for nanoparticles alone were found to be 0.59±0.02 and 2.60±0.02 ms respectively while the corresponding lifetime values for the complex were 0.37±0.03 and

2.10±0.05 ms respectively (fast:slow amplitude ratio of 1:3). Thus the fast component had a 37% faster decay while the slower component showed a 19% faster decay in the complex compared to luminescence lifetimes in the nanoparticles alone. As both time constants decreased concomitantly it is therefore not an artefact of the multi-exponential fitting procedure, rather enhanced de-excitation. Further, by restricting the time interval from 0.5–9.7 ms, i.e. collecting data from 0.5 ms after the UV excitation pulse, luminescence lifetimes could be modelled by mono-exponential decays that were 0.29 ms faster for the nanoparticle-containing complex than for nanoparticles alone, again showing enhanced de-excitation of the excited nanoparticles when they were part of the antibody-F_{ab}-AF-okadaic acid complex. These lifetime data are consistent with data recorded for analogous lanthanide systems such as europium chelates and Cy5 organic dye, suggesting that the fast decay component may be related to intramolecular energy transfer while the long component is related to the nanoparticle donor only [36]. In addition to lack of an AF fluorescence peak from the detection complex in the absence of okadaic acid, no shortening of luminescence lifetimes was noted for the nanoparticles bound only to antibodies or for nanoparticles bound to F_{ab}-AF labelled antibodies.

Analytical performance of the sensor

The intensity ratio of AF : LaNP emission peaks at 516 nm and 487 nm, respectively, with respect to okadaic acid concentration showed an excellent fit (R^2 = 0.994) to a sigmoidal curve based on the Boltzmann function $y = A2 + (A1-A2)/(1+\exp((x-x_0)/dx))$, where A1 was 0.080, A2 was 0.112, x_0 was 1.978 and dx was 0.692, in the okadaic acid concentration ([OA]) range from 0.25–5.95 μM (Figure 6a). A linear response of the intensity ratio to okadaic acid concentration ($y = 0.008[OA] + 0.079$; R^2 = 0.994) was determined for okadaic acid in the concentration range from 0.37–3.97 μM (Figure 6a, inset) and a limit of detection

of 0.25 µM was calculated. In contrast, interrogation of the nanoparticle-antibody-F_{ab}-AF complex in the absence of okadaic acid did not result in any fluorophore emission peak at 516 nm suggesting both that binding of okadaic acid was necessary for resonance energy transfer to occur and off-peak excitation of the fluorophore was below the instrumental detection limit. In addition, this ratiometric approach offers the advantage that it is essentially independent of the absolute concentration of the sensor.

The biosensor was tested on extracts of healthy mussel tissue and only background fluorescence was noted (No OA; Figure 8). Fluorescence from extracts of mussel tissue contaminated with okadaic acid was also determined and again only low level background fluorescence was noted from the crude extracts alone (No sensor; Figure 8). For a mixture of OA-contaminated extract and sensor in which the nanoparticle-bound antibody was intentionally omitted (i.e. only nanoparticle/F_{ab}-AF mixture present) to test for non-specific binding (No antibody; Figure 8). However, the fluorescence intensity ratio (I_{516}/I_{487}) for the combined extract and complete biosensor was much greater for various quantities of extracted mussel tissue than the two control samples, and the fluorescence intensity ratio increased with quantity of okadaic acid extracted from the homogenate. The extract average fluorescence intensity ratios for 50 mg, 100 mg and 300 mg homogenates were 23%, 19% and 27% lower (after background subtraction) than that expected from the idealized case (Figure 6a) and is likely due to the simplified and rapid extraction process used here not achieving maximum theoretical 100% okadaic acid retrieval. However, even efficient methods have shown losses of more than 18% okadaic acid as an artefact of the extraction process [37]. Thus optimization of the extraction method and use of a greater mass of mussel tissue homogenate would be expected to increase extraction yield values to greater than 90%. In addition, these calculations assume that the certified okadaic acid-contaminated mussel tissue has a

homogeneous distribution of okadaic acid throughout the tissue, whereas any inhomogeneity would likely give rise to deviations of the sensor response from that theoretically expected. However, a high correlation coefficient between the measured and expected values of 0.933 was noted, the biosensor thereby showing an appropriate fluorescence response with respect to increasing okadaic acid concentration in the environmental samples.

Ultimately, sensitivity to very low levels of okadaic acid, as defined by the regulatory environment, is one of the most important aspects in the development of biotoxin sensors. In this case, the situation is more complex as the current European food safety limit of 160 μgOA kg^{-1} shellfish meat (approximately 160 adult mussels yield 1 kg meat, hence 1 μgOA mussel^{-1}) is several times higher than the acute dose response, so any future reduction of the safety limit must be taken into consideration with respect to sensor development. For example, a reduced regulatory limit of 40 μgOA kg^{-1} shellfish meat is the equivalent of approximately 250 ngOA per individual mussel and a demonstration of sensitivity to OA at levels lower than this is a necessary requirement for the technique to be considered promising. In this work, a lower detection limit in the linear response range was calculated to be 200 ngOA ml^{-1} (0.25 μM; this mass of okadaic acid being equivalent to 32 μgOA kg^{-1} assuming equal quantity of okadaic acid in 160 mussels), a value lower than potential future safety limits, suggesting that the technique may be potentially sensitive enough to be applied at the individual mussel level. The values in this work also compare favourably with other optical biosensors, as for example the recent application of a surface plasmon resonance (SPR) biosensor chip for okadaic acid group of toxins gave a slightly lower limit of detection of 31 μgOA kg^{-1} and a sensor working range of 31-174 μgOA kg^{-1} (equivalent to 0.24-1.36 μM OA in our system while our linear response range was 0.37-3.97 μM) [17]. However it should be noted that the sensor in that work was developed to codetect dinophysistoxin-1

18

(DTX-1), DTX-2 and DTX-3 with okadaic acid, hence the response range would be expected to vary from that reported in our work. Other authors have also discussed using SPR based techniques for okadaic acid determination and have reported similar working ranges of 2-2000 µg kg^{-1} [16] and 20-320 µg kg^{-1} [38] while the recent application of microfluidics devices has enabled the extremely low range of 2-18 nM to be accessed [39], the latter showing sensitivity two orders of magnitude greater than our work.

While optical biosensors based on chip technology are becoming increasingly popular, much work on biosensors has also been reported over the past number of years on demonstrating the ability to generate a FRET signal based on molecular recognition and binding. Often, these systems rely on the binding of highly selective moieties with extremely high affinity such as the biotin-streptavidin pair to bring donors and acceptors sufficiently close to enable resonance energy transfer [40] and [41]. In contrast, this work reports on the use of polyclonal antibodies to provide the key recognition and binding step for the optical detection of okadaic acid. The use of polyclonal antibodies has disadvantages in some cases, particularly lack of specificity issues in multi-parametric assays where there may be unwanted cross-reactivity when attempting to distinguish among very similar toxin congeners. In such cases more selective monoclonal antibodies or highly selective synthetic oligonucleotide sequences (aptamers) may be used [42]. However, from the perspective of determining the total toxic potential of a sample, particularly in a regulatory environment, it is less important in the first instance to differentiate among toxin congeners which show only minor structural variations but still produce the same toxic response. Thus the ability of polyclonal antibodies to tolerate minor variations of the 'parent' toxin and bind multiple epitopes may offer a distinct advantage in this case.

Conclusions

We have shown for the first time the ability to use simple mix and shake solution chemistry based on luminescent nanoparticles and molecular recognition to achieve an optical response to the presence of okadaic acid biotoxin. The method does not require sophisticated peak deconvolution and may be sufficiently sensitive and versatile to become a complementary technique to high performance chromatographic methods for detecting biotoxins. Further, the technique is not necessarily limited to the detection of individual toxin classes but may be extended to simultaneously detect a range of biotoxin classes. Such a multi-parametric sensor may be based on a composite solution of different nanoparticle-dye pairs which are reactive towards different biotoxins or by using a single type of nanoparticle but with various dyes which give spectral overlap with the different emission lines of the nanoparticle, e.g. separate dyes which would overlap with the 490 nm and 540 nm emission lines of the lanthanide nanoparticles used in this work. However, much work is still required, and in particular a fuller characterization of the system, so as to allow the future rational design of such biosensors. For example, determining the specific orientation of the antibodies with respect to the nanoparticle and the location of the area of the protein that is binding to the nanoparticle will allow better estimation and tailoring of donor-acceptor distances to achieve the desired energy transfer process. The technique may ultimately be modified to give greater sensitivity towards specific molecules or epitopes within a biotoxin class by using aptamers in place of antibodies. However, the nature of the linkage between a labelled aptamer and nanoparticle is likely to be crucial, for example a flexible linker is required to allow a conformation change (such a conformation change functionality may have to be built into the linker) upon binding to the target while too flexible a linker may bring donor and acceptor too close giving rise to resonance energy transfer even in the absence of the target molecule. Ultimately, these systems show great promise as a new tool not only for food and

20

environmental monitoring, but eventually even in diagnostic tests for other biomolecules of interest in human health care.

References

[1] Dawson, J. F.; Holmes, C. F. B. *Front. Biosci.* **1999**, *4*, 646-658.

[2] Jang, D. -J.; Guo, M.; Wang, D. J. *Proteome Res.* **2007**, *6*, 3718–3728.

[3] Valdiglesias, V.; Laffon, B.; Pásaro, E.; Méndez, J. *J. Environ. Monit.* **2011**, *13*, 1831-1840.

[4] Yasumoto, T.; Murata, M. *Chem. Rev.* **1993**, *93*, 1897-1909.

[5] Council Directive 86/609/EEC of 24 November 1986; E.E.C.: Brussels, 1986.

[6] *Report of the Joint FAO/IOC/WHO ad hoc Expert Consultation on Biotoxins in Bivalve Molluscs*; F.A.O.: Oslo, Norway, 2004.

[7] Scientific Opinion of the Panel on Contaminants in the Food Chain on a Request from the European Commission on Marine Biotoxins in Shellfish. *EFSA J.* **2009**, *1306*, 1-23.

[8] Fischer, W.; Garthwaite, I.; Miles, C.; Ross, K.; Aggen, J.; Chamberlin, R.; Towers, N.; Dietrich, D. *Environ. Sci. Technol.* **2001**, *35*, 4849-4856.

[9]   Rapala, J.; Erkomaa, K.; Kukkonen, J.; Sivonen, K.; Lahti, K. *Anal. Chim. Acta* **2002**, *466*, 213-231.

[10]   Comesanã-Losada, M.; Gago-Martínez, A.; Leao-Martins, J. M.; Rodríquez-Vázquez, J. *Analyst* **1996**, *121*, 1665-1670.

[11]   Campàs, M.; Garibo, D.; Prieto-Simón, B. *Analyst* **2012**, *137*, 1055-1067.

[12]   Wang, X.-H.; Wang, S. *Sensors* **2008**, *8*, 6045-6054.

[13]   Tang, A. X. J.; Kreuzer, M.; Lehane, M.; Pravda, M.; Guilbault, G. G. *Int. J. Environ. Anal. Chem.* **2003**, *83*, 663-670.

[14]   Campàs, M.; de la Iglesia, P.; Le Berre, M.; Kane, M.; Diogène, J.; Marty, J.-L. *Biosens. Bioelectron.* **2008**, *24*, 716-722.

[15]   Prieto-Simón, B.; Miyachi, H.; Karube, I.; Saiki, H. *Biosens. Bioelectron.* **2010**, *25*, 1395-1401.

[16]   Marquette, C.; Coulet, P.; Blum, L. J. *Anal. Chim. Acta* **1999**, *398*, 173-182.

[17]   Stewart, L. D.; Hess, P.; Connolly, L.; Elliott, C. T. *Anal. Chem.* **2009**, *81*, 10208-10214.

[18]   Fitter, J.; Katranidis, A.; Rosenkranz, T.; Atta, D.; Schlesinger, R.; Büldt, G. *Soft Matter* **2011**, *7*, 1254-1259.

[19]   Sammes, P. G.; Yahioglu, G. *Nat. Prod. Rep.* **1996**, *13*, 1-28.

[20]   Eliseeva, S. V.; Bünzli, J.-C. G. *Chem. Soc. Rev.* **2010**, *39*, 189-227.

[21]   Van Veggel, F. C. J. M.; Dong, C.; Johnson, N. J. J.; Pichaandi, J. *Nanoscale* **2012**, *4*, 7309-7321.

[22]   Liu, Y.; Tu, D.; Zhu, H.; Chen, X. *Chem. Soc. Rev.* **2013**, *42*, 6924-6958.

[23]   Li, Z.; Sun, Q.; Zhu, Y.; Tan, B.; Xu, X. P.; Dou, S. X. *J. Mater. Chem. B* **2014**, *2*, 2793-2818.

[24]   Diamente, P. R.; Burke, R. D.; van Veggel, F. C. J. M. *Langmuir* **2006**, *22*, 1782-1788.

[25] Mattoussi, H.; Mauro, J. M.; Goldman, E. R.; Anderson, G. P.; Sundar, V. C.; Mikulec, F. V.; Bawendi, M. G. *J. Am. Chem. Soc.* **2000**, *122*, 12142-12150.

[26] Armstrong, J. K.; Wenby, R. B.; Meiselman, H. J.; Fisher, T. C. *Biophys. J.* **2004**, *87*, 4259-4270.

[27] Calzolai, L.; Franchini, F.; Gilliland, D.; Rossi, F. *Nano Lett.* **2010**, *10*, 3101-3105.

[28] Casanova, D.; Giaume, D.; Moreau, M.; Martin, J.–L.; Gacoin, T.; Boilot, J.-P.; Alexandrou, A. *J. Am. Chem. Soc.* **2007**, *129*, 12592-12593.

[29] Tokarova, V.; Pittermannova, A.; Kral, V.; Rezacova, P.; Stepanek, F. *Nanoscale* **2013**, *5*, 11490-11498.

[30] Bunzli, J.-C. G.; Eliseeva, S. *Chem. Sci.* **2013**, *4,* 1939-1949.

[31] Binnemans, K. *Chem. Rev.* **2009**, *109*, 4283-4374.

[32] Horrocks Jr., W. DeW.; Sudnick, D. R. *J. Am. Chem. Soc.* **1979**, *101*, 334-340.

[33] Janeway, C. A., Jr.; Travers, P.; Walport, M.; Shlomchik, M. J. *Immunobiology: The Immune System in Health and Disease*, Garland Science: New York, 2005; Chapter 3, pp 103-134.

[34] Bünzli, J.-C. G. In *Lanthanide Probes in Life, Chemical and Earth Sciences: Theory and Practice*, Bünzli, J.-C. G., Choppin, G. R., Eds., Elsevier: Amsterdam, 1989; Chapter 7, pp 219-294.

[35] Casanova, D.; Giaume, D.; Gacoin, T.; Boilot, J. P.; Alexandrou, A. J. *J. Phys. Chem. B* **2006**, *110*, 19264-19270.

[36] Selvin, P. R.; Rana, T. M.; Hearst, J. E. *J. Am. Chem. Soc.* **1994**, *116,* 6029-6030.

[37] Croci, L.; Draisci, R.; Lucentini, L.; Cozzi, L.; Giannetti, L.; Toti, L.; Stacchini, A. *Toxicon* **1995**, *33*, 1511-1518.

[38] Llamas, N. M.; Stewart, L.; Fodey, T.; Cowan Higgins, H.; Velasco, M. L. R.; Botana, L. M.; Elliott, C. T. *Anal. Bioanal. Chem.* **2007**, *389*, 581–587.

[39] Campbell, K.; McGrath, T.; Sjolander, S.; Hanson, T.; Tidare, M.; Jansson, O.; Moberg, A.; Mooney, M.; Elliott, C.; Buijs, J. *Biosens. Bioelectron.* **2011**, *26*, 3029–3036.

 [40] Menéndez, G. O.; Pichel, M. E.; Spaqnuolo, C. C.; Jares-Erijman, E. A. *Photochem. Photobiol Sci.* **2013**, *12*, 236-240.

[41] D′Hooge, F.; Elfeky, S. A.; Flower, S. E.; Pascu, S. I.; Jenkins, A. T. A.; van den Elsen, J. M. H.; James, T. D.; Fossey, J. S. *RSC Adv.* **2012**, *2*, 3274-3280.

[42] Cho, E. J.; Lee, J.-W.; Ellington, A. D. *Ann. Rev. Anal. Chem.* **2009**, *2*, 241-264.

Figures
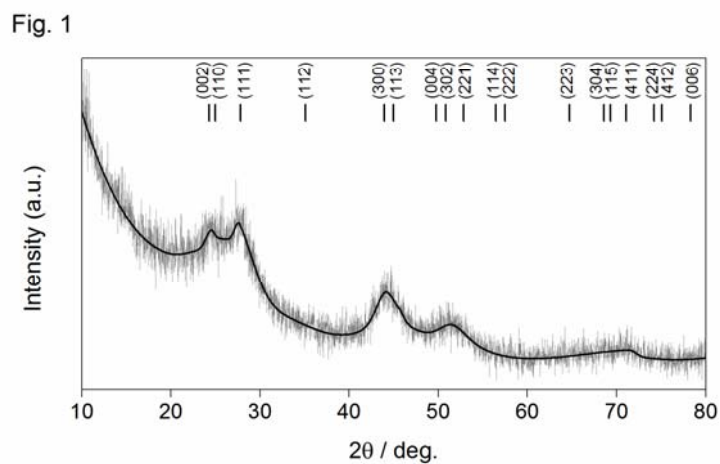
Figure 1.   Powder X-ray diffractogram of dry lanthanide nanoparticles (grey line) and fitted pattern (black line) based on a hexagonal LaF_3 phase (crystal planes labelled).

Fig. 2
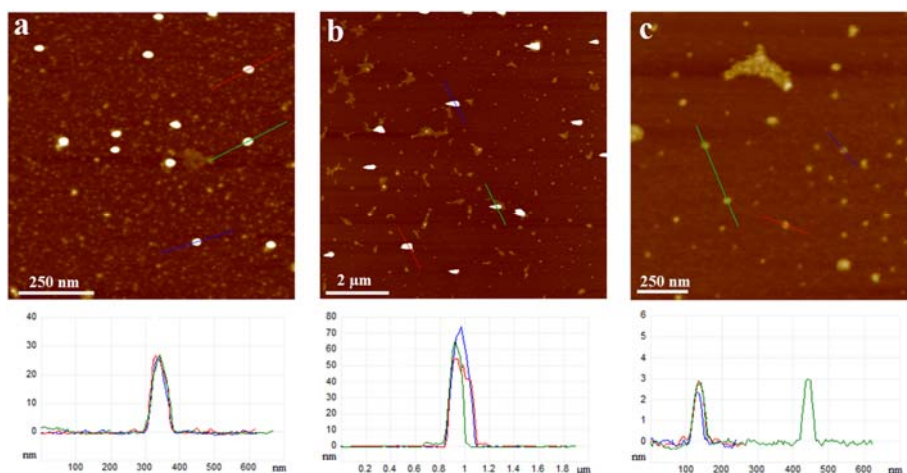
Figure 2.   AFM images of (a) lanthanide nanoparticles, (b) nanoparticle-antibody conjugates and (c) anti-okadaic acid antibodies, with height profiles along indicating lines. Images were acquired in tapping mode.

Fig. 3
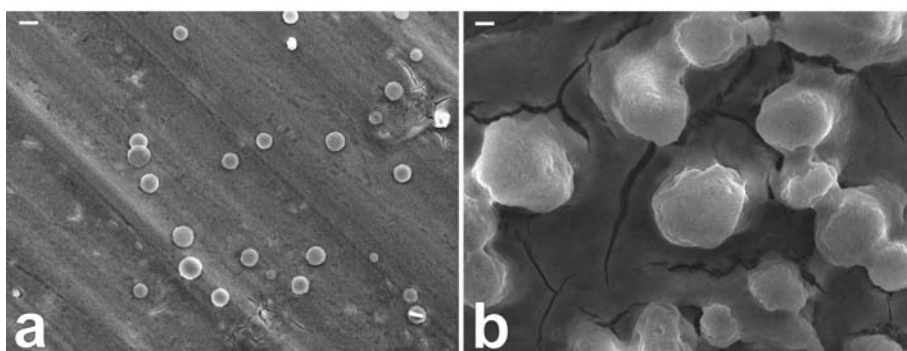
Figure 3.   Scanning electron micrographs of dehydrated samples of (a) lanthanide nanoparticles and (b) nanoparticle-antibody conjugates. Scale bar = 1 μm.
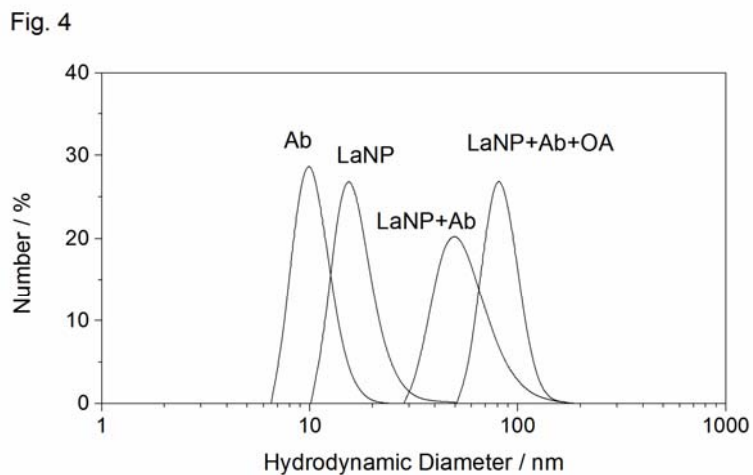
Figure 4.   DLS number size distribution for anti-okadaic acid antibodies (Ab), lanthanide nanoparticles (LaNP), nanoparticle-antibody-F_{ab}-AF (LaNP+Ab) and nanoparticle-antibody-F_{ab}-AF-okadaic acid (LaNP+Ab+OA) complexes
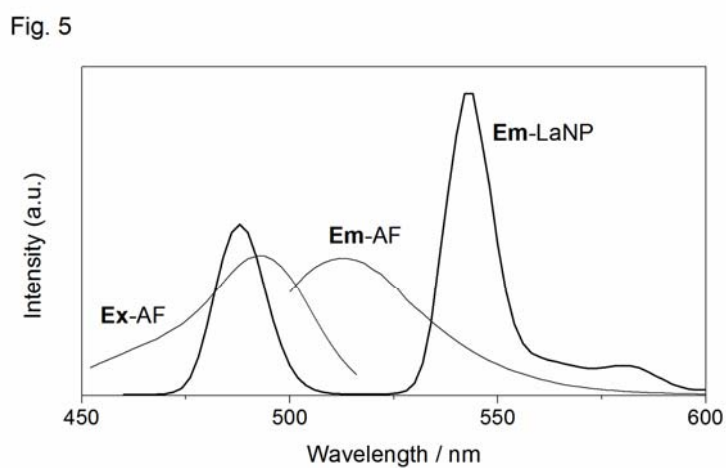
Figure 5.   Excitation (Ex) and emission (Em) spectra of the lanthanide nanoparticle (LaNP) donor and AlexaFluor488 (AF) acceptor

Fig. 6a
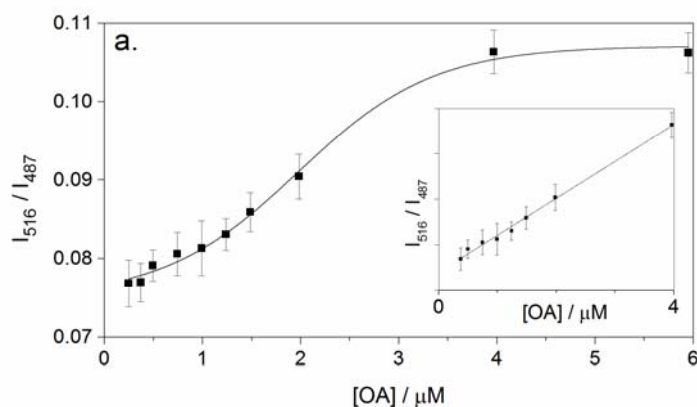
Fig. 6b
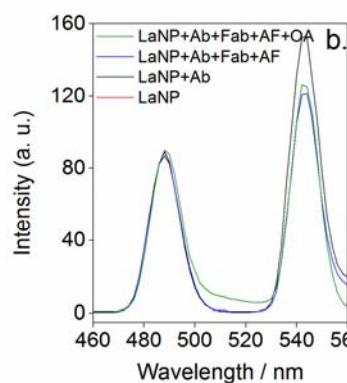
Fig. 6c
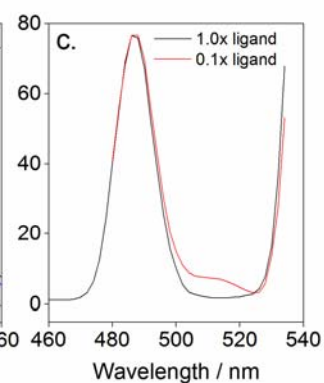
Figure 6   (a) Ratio of emission intensities for AlexaFluor488 acceptor (I_{516}) and lanthanide nanoparticle donor (I_{487}) with increasing okadaic acid (OA) concentration. Inset: corresponding fit of data in the linear range. Error bars indicate standard deviations (n=3). (b) Emission spectra for various sensor fragments comprising of nanoparticles (LaNP), antibodies (Ab), AlexaFluor-labelled F_{ab} (F_{ab}-AF) and okadaic acid (OA). (c) Emission spectra of the LaNP-Ab-F_{ab}-AF sensor in the absence of okadaic acid, where the nanoparticle was synthesized with normal (1.0× ligand) and 10 times less (0.1× ligand) amount of *o*-phosphorylethanolamine ligand.
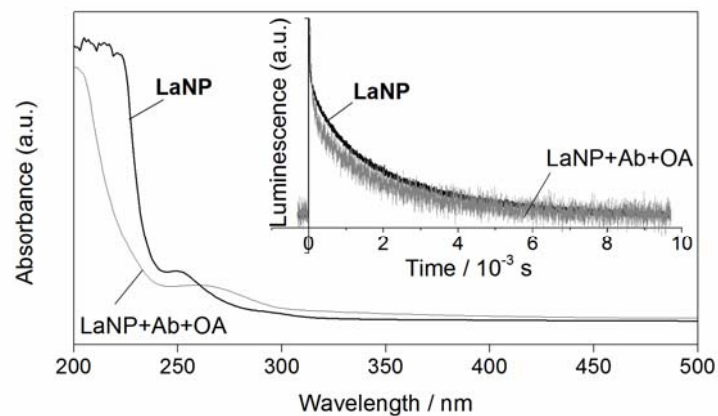
Figure 7. Absorption spectra for lanthanide nanoparticles (LaNP; dark line) and nanoparticle-antibody-F_{ab}-AF-okadaic acid complex (LaNP+Ab+OA). Inset: luminescence decay of LaNP (dark line) and LaNP+Ab+OA after excitation at 266 nm.
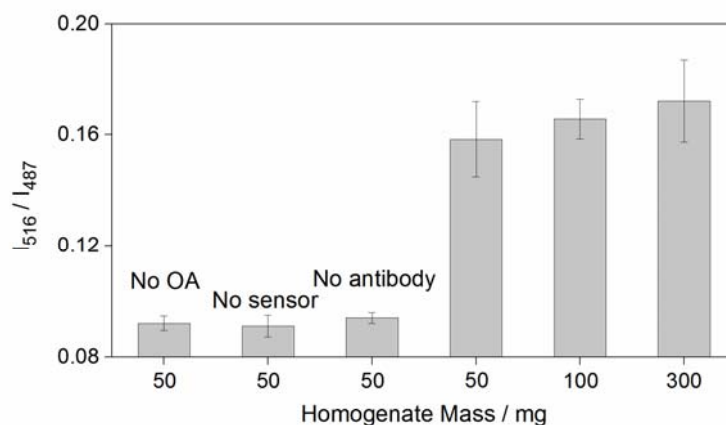

Figure 8. Fluorescence intensity ratio for biosensor-extract mixture for various quantities of extracted mussel tissue homogenate. Error bars indicate standard deviations (n=3).
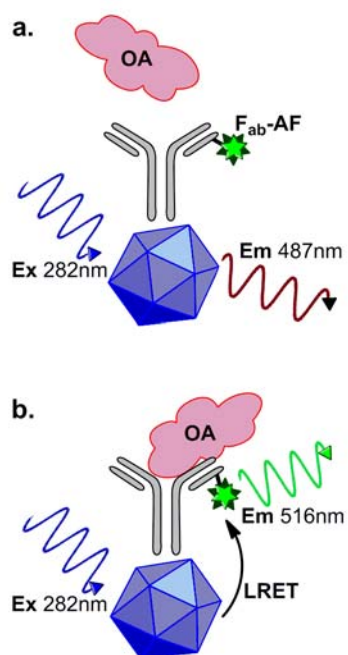
Scheme 1.   (a) Excitation and emission from lanthanide nanoparticles (LaNP) decorated with F_{ab}-Alexafluor488 (F_{ab}-AF) labelled antibodies in the absence of okadaic acid. (b) Luminescence resonance energy transfer between LaNP donor and AF acceptor, and emission at longer wavelength, upon okadaic acid-antibody binding.